Two-step growth mechanism of supported Co_3O_4-based sea-urchin like hierarchical nanostructures

Chiara Maurizio[a,*], Raju Edla[b], Niccolo' Michieli[a], Michele Orlandi[b], Angela Trapananti[c], Giovanni Mattei[a], Antonio Miotello[b]

[a] *Physics and Astronomy Department and CNISM, University of Padova, via Marzolo 8, I-35131 Padova, Italy*
[b] *Physics Department, University of Trento, via Sommarive 14, 38123 Povo (Trento), Italy*
[c] *CNR-IOM, Physics and Geology Department, University of Perugia, Italy*

Abstract

Supported 3D hierarchical nanostructures of transition metal oxides exhibit enhanced photocatalytic performances and long-term stability under working conditions. The growth mechanisms crucially determine their intimate structure, that is a key element to optimize their properties. We report on the formation mechanism of supported Co_3O_4 hierarchical sea urchin-like nanostructured catalyst, starting from Co-O-B layers deposited by Pulsed Laser Deposition (PLD). The particles deposited on the layer surface, that constitute the seeds for the urchin formation, have been investigated after separation from the underneath deposited layer, by X-ray diffraction, X-ray absorption spectroscopy and scanning electron microscopy. The comparison with PLD deposited layers without O and/or B indicates a crucial role of B for the urchin formation that (i) limits Co oxidation during the deposition process and (ii) induces a chemical reduction of Co, especially in the particle core, in the first step of air annealing (2 h, 500 °C). After 2 h heating Co oxidation proceeds and Co atoms outdiffuse from the Co fcc particle core likely through fast diffusion channel present in the shell and form Co_3O_4 nano-needles. The growth of nano-needles from the layer beneath the particles is prevented by a faster Co oxidation and a minimum fraction of metallic Co. This investigation shows how diffusion mechanisms and chemical effects can be effectively coupled to obtain hierarchical structures of transition metal oxides.

1. Introduction

Composites based on hierarchical nanostructures of transition metal oxides are very promising materials for various photocatalytic applications, including degradation of pollutants, H_2 production and CO_2 reduction [1, 2]. Their peculiar structure boosts light scattering and harvesting, largely increases the surface

*Corresponding author
Email address: chiara.maurizio@unipd.it (Chiara Maurizio)

area and can improve the diffusion of reactant molecules, further enlarging the accessible photocatalyst active area [1, 3]. With respect to hierarchical nanostructures in form of powder, supported hierarchical nanostructures do not suffer from agglomeration and during operation are not dispersed in the environment. This offers a great practical advantage, allowing reuse and operation under continuous flow [4, 5, 6]. The control of the hierarchical morphology is a key element to optimize the catalytic performance [7]. The growth of nanowires, nanopetals and nanoneedles of transition metal oxide can be effectively induced by thermal oxidation of a metallic (or not completely oxidized) structure [8, 9, 10]. Despite the number of papers published on the subject, the details of the formation process of 3D hierarchical nanostructures are not completely unveiled, especially when thermal diffusion and chemical reactions are both operating to promote nanostructuring of a preexisting system. The formation of Co-oxide nanowires and nanopetals from metallic Co by oxidizing annealing (350-520 °C) has been suggested to be related to the melting of a thin surface layer (formed of metallic Co or CoO), favoring oxygen dissolution in the liquid and the subsequent precipitation [11, 12, 13]. While the mobility of the surface (ad)atoms can be important even at low temperature, the hypothesis of a lowering of more than 1000 K of the melting point of the surface layer should deserve further experimental proof. In some other cases, the growth of nanoneedles forming urchin-like nanostructures of transition metal oxides (α-Fe_2O_3) has been explained as a selective directional growth via inter-diffusion of oxygen and metal atoms from the metallic core of the particle [9]. Certainly, in presence of more than one oxidizable species, the enthalpy of formation of the different oxides involved has to be taken into account, also considering that in principle the chemical oxidation of one species can determine the chemical reduction of the other.

We have recently shown that supported Co_3O_4 3D sea urchin-like nanostructures, formed by pulsed laser deposition of Co-O-B layers upon heating in air [4], exhibit an enhanced photocatalytic activity for degradation of methylene blue dye. They also show an exceptional long-term stability, largely superior to similar systems prepared by hydrothermal route [4]. Starting from this promising photocatalytic result, we address here a full structural investigation to unveil the complex growth mechanism of these 3D hierarchical nanostructures. The results presented are based on scanning electron microscopy, X-ray diffraction and X-ray absorption spectroscopy, allowing to get a full picture on both the amorphous and crystalline phases involved in the growth process [14, 15, 16, 17]. The investigation of both the full deposited layer and separately of the surface particles that constitute the seed for the urchins formation allowed to shed light on a complex growth process, showing how diffusion mechanisms and chemical effects can be effectively coupled to obtain hierarchical structures of transition metal oxides.

2. Experimental and data analysis

Co-O-B layers were deposited on glass substrates by Pulsed Laser Deposition (PLD), using cold-pressed pellets of Co-B powder as the target, room-temperature and an O_2 atmosphere. The precursor Co-B powder was synthesized according to literature [18]. PLD was carried out using a KrF excimer laser (Lambda Physik) at an operating wavelength of 248 nm, pulse duration of 25 ns, and repetition rate of 20 Hz. The laser fluence was set at 3 J/cm^2 and target-to-substrate distance at 4.5 cm. A more detailed description of the PLD deposition apparatus is reported elsewhere [19]. The PLD chamber was evacuated up to a base pressure of 10^{-6} mbar prior to the deposition, a reactive O_2 atmosphere (pressure of 4.5 x 10^{-2} mbar) was then kept constant during the experiment. The same conditions were employed for Co-O layers PLD deposition ('Co-O layer'), with the exception of the target, which in this case was a pure (Sematrade, 99.9%) metallic Co disk. In the case of Co coatings, the target was a a pure (Sematrade, 99.9%) metallic Co disk and deposition was performed in vacuum at the baseline pressure.
PLD deposition promoted the formation of an uniform deposited layer with nestled spheroidal particles in a wide range of size, from 10 nm to few micrometers [4]. The deposited layers were annealed in air in a tubular oven at 500 °C for definite time intervals up to 4 hours. The structural investigations where first carried out on the obtained full layers. Then, each layer was covered with a commercial liquid polyurethane (NOA61 from Norland, labelled 'NOA' in the following) and after UV-induced polymerization, the polymer was peeled off from the substrate. During this procedure, as sketched in Figure 1, part of the spheroidal particles remains embedded in the NOA polymer. In this way they could easily be handled and characterized. In the following, the PLD deposited layers are named 'full layers', while the urchins and the spheroidal particles embedded in the NOA polymer are named 'particle layer'.

Scanning Electron Microscopy (SEM) measurements were carried out with a

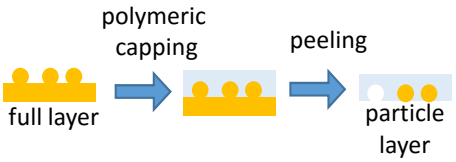

Figure 1: (Color online) Sketch of the procedure used to separate the Co-O-B particles from the underneath Co-O-B deposited layer.

Zeiss Sigma HD SEM, equipped with InLens, Secondary Electrons (SE) and Backscattered Electrons (BSE) detectors for the imaging, with a spotsize of 1 nm. Energy Dispersive X-ray spectroscopy (EDX-SEM) was performed by recording the fluorescence emission from the samples. The EDX system was an INCA x-art by Oxford, equipped with a Silicon Drift Detector with a nominal

resolution of 129 eV at 5.9 keV.

Grazing Incidence X-Ray Diffraction (GIXRD) spectra were collected with a X'Pert Pro diffractometer (incidence angle = 1 deg), using the Cu K_α radiation. The GIXRD analysis was performed by using the MAUD software [20].

Co K-edge X-ray absorption spectroscopy (XAS) experiment (both EXAFS-Extended X-ray Absorption Fine Structure and XANES-X-ray Absorption Near-Edge Structure) was performed at the Italian beamline BM08 of the European Synchrotron-ESRF (Grenoble, F). The monochromator was equipped with a couple of Si (311) crystals, working in dynamic sagittal focusing configuration. A couple of Pd-coated mirrors (incidence angle = 3.6 mrad) were used to reject harmonics and to vertically focus the x-ray beam on the sample. XAS spectra were measured at room temperature in fluorescence mode by a 12-element high purity Ge detector. XAS spectra of metallic Co foil, of crystalline powder pellets made of CoO (octahedrally coordinated Co^{2+}), $Co(C_5H_7O_2)_3$ (octahedrally coordinated Co^{3+}) and Co_3O_4 were also measured in transmission mode as standard references. In all cases a reference spectrum of Co metal was recorded just before and just after each spectrum, to ensure a correct energy calibration (the maximum of the first derivative of the Co foil absorption spectrum was set as 7709 eV). XAS analysis was performed by using the FEFF8-FEFFIT package [21].

3. Results

In Figure 2(a-d) the SEM images of the PLD deposited layers, annealed for different time intervals at 500 °C are shown. SEM images of two representative layers recorded at lower magnification are reported in Figure 2(e,f). On a porous layer, spheroidal particles are visible in all cases. After 1 h annealing, both the spheroidal particles and the underneath substrate present a rough surface. Starting from about 2 h annealing the growth of nano-needles at the surface of the particles (not on the layer below) is visible, that resemble microscopic sea-urchins.

Figure 2(g) shows an example of secondary electrons SEM image of an urchin (formed after 4 h annealing) embedded in the polymer after the peeling procedure. The urchin-like morphology is preserved inside the polymeric matrix. Small voids are visible in the particle core, suggesting that part of the material outdiffused during the annealing, as also observed for specific annealing conditions of similar systems [17, 22]. The signal of the backscattered electrons from the same region is shown in Figure 2(h). In this case, brighter zones indicate higher Z elements, so that the compositional contrast between the Co-based urchin (higher electronic density) and the surrounding polymer is well visible. EDX-SEM was performed on selected spots, giving the two X-ray fluorescence spectra shown in Figure 2(i). The red spectrum was acquired in a region where only the NOA polymer was probed by the 10 KeV electron beam, showing the fluorescence lines from sulfur, oxygen and carbon (the components of NOA).

The black spectrum was recorded on the particle, showing in addition the characteristic lines of cobalt and confirming the presence of urchins in the polymer.

In Figure 3(a) the GIXRD spectra of the PLD deposited layers (full lay-

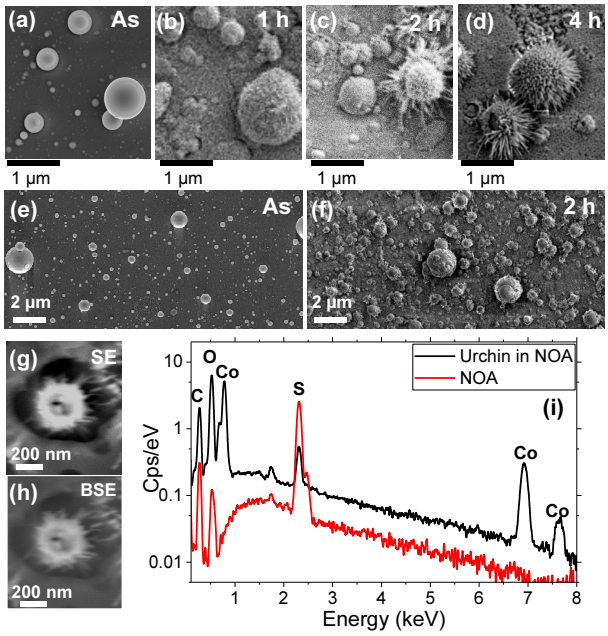

Figure 2: (a-f) SEM images of the deposited full layers annealed at 500 °C in air for different time intervals: (a,e) as-deposited layer, (b) 1 h-annealed layer, (c,f) 2 h-annealed and (d) 4 h-annealed layer. (g,h) SEM images of an urchin embedded in the NOA polymer after peeling, obtained by recording the signal of (g) secondary electrons (SE) or (h) backscattered electrons (BSE). (i) EDX-SEM spectra of NOA (red) and of an urchin embedded in NOA (black). The black spectrum shows the fluorescence lines of Co atoms in addition to those of the NOA components (S,O,C).

ers) annealed at 500 °C in air are reported for different annealing intervals, and compared to the spectrum for the as-deposited layer. The spectrum recorded after 600 °C annealing for 4 h (complete Co oxidation [4]) is also reported for comparison. The XRD signal from the as-deposited full layer is rather low, indicating that the most part of the layer is amorphous. The minor crystalline fraction arises from Co fcc and likely Co_2B [23]. The air annealing promotes a progressive crystallization. After 2 h annealing, two main crystalline phases are well visible, namely, Co_3O_4 (average crystallite size of about 15 nm) and fcc metallic Co (average crystallite size of about 50 nm). A faint signal of CoO is also barely visible (peak at $2\theta = 42$ deg). The crystallization of Co_3O_4 proceeds with the annealing time and this phase constitutes the most relevant signal starting from 3 h annealing (maintaining about the same average crystallite size).

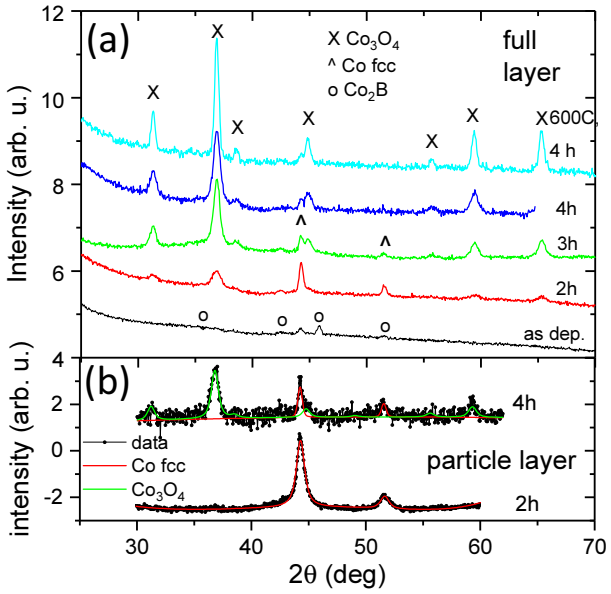

Figure 3: (Color online) (a) GIXRD patterns for the PLD deposited full layers, heated in air at 500 °C in air for the indicated time. The GIXRD spectrum of a layer annealed at 600 °C for 4 h is also reported for comparison. The peak positions for Co fcc, Co_3O_4 and Co_2B are marked. (b) GIXRD patterns for peeled-off layers, obtained by Co-O-B deposited layers annealed in air at 500 °C as indicated.

Conversely, the intensity of Co fcc phase increases in the first 2 h annealing and then progressively vanishes. After 4 h annealing at 600 °C the only crystalline phase detected is Co_3O_4. No crystalline signal related to boron oxides has been detected in the investigated layers.

In Figure 3(b) the GIXRD spectra recorded on the particles embedded in the polymer are reported. Since the amount of material embedded in the polymer is quite low, we could obtain significant diffraction patterns only for the annealed layers. Nevertheless, as shown later on, the procedure used is effective for the XAS analysis of the all the samples. The GIXRD spectra of the particle layers indicate that after 2 h annealing the only crystalline signal from the spheroidal particles is from metallic Co, while for longer annealing intervals the fraction of metallic Co decreases and the Co_3O_4 signal increases. The comparison between the signal from the full layers and corresponding particle layers indicates that the most part of the crystalline material is located in the layer beneath the particles. In Figure 4 the crystalline fractions of the different phases measured for the full layers and for the particle layers are reported. For the full layers, the normalization of the crystalline fraction has been done with respect to the total diffracted signal intensity of the 4h-annealed layer. In both kinds of layers (i.e., full layers and particle layers) the Co_3O_4 fraction progressively increases with the annealing time. Nevertheless, while it represents the major crystalline

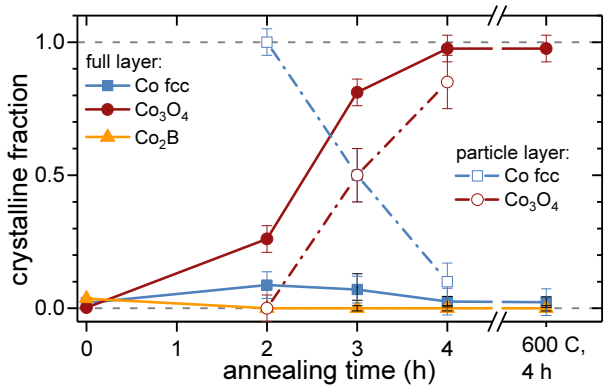

Figure 4: (Color online) Evolution of the different crystalline phases with the annealing time, at 500 °C (solid line: full layers, dashed line: particle layers). For the full layers only, the crystalline fraction is normalized to the crystalline signal measured after 4 h annealing.

phase after 2h heating of the full layer, it is below the detectable limit for the particle layer. Moreover, for a definite annealing duration, the relative fraction of metallic fcc Co is higher in the particle layer with respect to the corresponding full layer. On the investigated crystalline part of the layer, the results suggest that part of the Co atoms first undergo a chemical reduction (in the first about 2 h) and then a chemical oxidation (after 2-4 h annealing).

In Figure 5 the XANES spectra measured at Co K-edge for the full layers and for the particle layers are compared for definite annealing durations. From the different features of the spectra, information can be obtained on the Co oxidation process and oxidation state, in particular by comparison with the reported spectra of relevant Co-based standard compounds. Indeed, while the onset of the photoelectric absorption is at 7709 eV for metallic Co, for Co oxides the absorption threshold (corresponding to half of the edge jump) is progressively shifted towards higher energy as the oxidation state increases. The small pre-edge peak in the region 'A' (at about 7710 eV) for Co oxides is related to a dipole allowed transition from the state 1s to mixed p-d orbital and is very low for a centrosymmetric Co site (i.e., octahedral) for which p-d mixing is not allowed. [15]. For the as-deposited particle layer the absorption spectrum (see Figure 5(a)) is similar to the one of Co foil (see in particular the absorption in the 'A' region, significantly higher than for the Co-oxides), indicating that a relevant fraction of Co is in the metallic state. For the as-deposited full layer, the low absorption in the 'A' region combined with the absorption threshold very close to the one of CoO indicate that the most part of Co is oxidized, with oxidation state 2+. The pre-edge peak is slightly higher than for CoO, suggesting a more disordered site (i.e., a non-centrosymmetric site) for Co ions. After 2 h annealing (Figure 5(b)) the absorption spectrum of the particle layer becomes even more similar to the one of Co foil, indicating that Co atoms in the particle layer are mostly metallic. Conversely, in the full layer Co atoms are

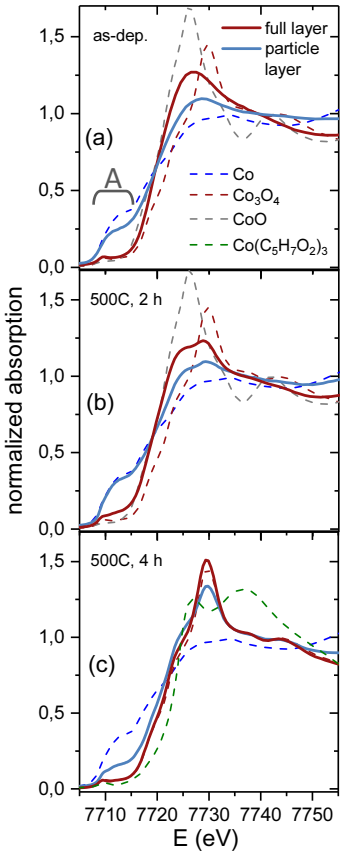

Figure 5: (Color online) XANES spectra of the samples (full layers and particle layers) obtained upon annealing at 500 °C for (a) 0 h (as-deposited samples), 2 h (b), 4 h (c). The spectra of Co_3O_4, metallic Co, CoO and $Co(C_5H_7O_2)_3$ are reported for comparison.

mostly oxidized, still with oxidation state 2+. After 4h annealing (Figure 5(c)) in the particle layer a fraction of metallic Co remains (the absorption coefficient in the 'A' region is still higher than for Co-oxide), while the spectrum of the full layer is the one of Co_3O_4 (also the pre-edge peak is very similar to the one of Co_3O_4).

In Figure 6(a) the Fourier transform moduli of the EXAFS spectra for the different samples (full layers and particle layers) are shown. They represent a pseudo-radial distribution function of atoms around the absorber, Co in this case, and the contributions of the first atomic shells around the average Co atom are visible. The spectra for Co_3O_4 and metallic Co are also shown.

Consider first the full layers. A first Co-O coordination is visible in all cases. A Co-Co metallic coordination is barely visible for annealing duration less than 2 h, and is present as a minor phase for the layer annealed for 2 h (the full

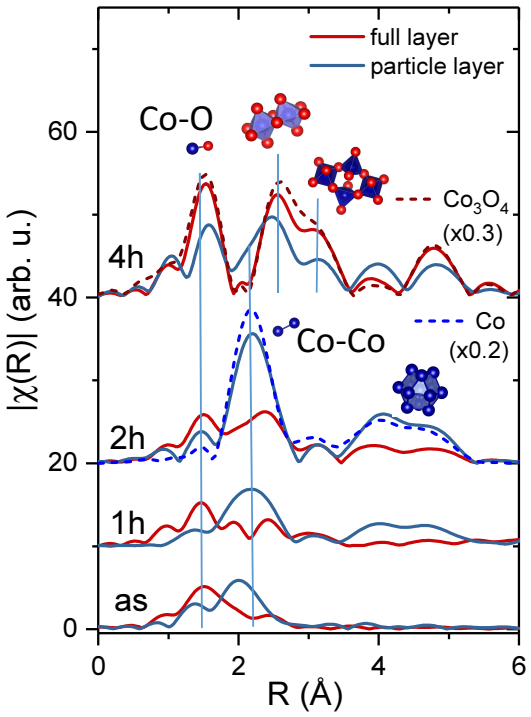

Figure 6: (Color online) Fourier transform moduli (in the range k=3-11Å^{-1}) of the EXAFS spectra for the full layers and particle layers, after different annealing times at 500 °C, compared to the spectra of pertinent standard references (Co_3O_4, Co foil). The vertical lines locate the position of the Co-Co single scattering peak for metallic Co and of Co-O peak for Co_3O_4. The location of the signals from the medium range structures of metallic Co and Co_3O_4 are also reported (see the Supplementary Material for details).

results are reported in the Supplementary Material). In this case, considering that XRD detected Co clusters of several nanometers (i.e., corresponding to a coordination number, CN, close to the bulk one), from the observed CN (Table S1) we can roughly estimate that the fraction of metallic Co after 2 h annealing is ≈10-20% (see Supplementary Material). After 4 h annealing, the spectrum is very similar to the one of Co_3O_4 and the intermetallic coordination is below the detectable limit for the technique.

As far as the particle layers are concerned, the Co-Co metal coordination is present for all the layers, from the as-deposited to the 4h-annealed one. The corresponding coordination number is significantly higher than for the full layer, although still lower than the one for metallic bulk Co. The signal from the Co-O coordination is also always visible. These findings indicate that (i) the fraction of metallic Co is higher in the particle layer with respect to the full layer, in

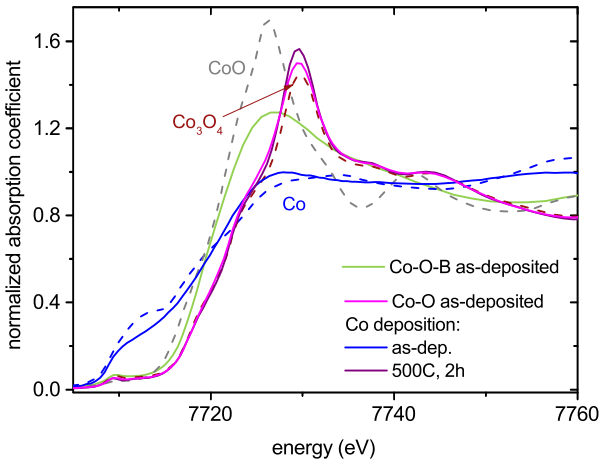

Figure 7: XANES spectra of the Co-deposited layer in O_2 atmosphere ('Co-O deposition') or in vacuum ('Co deposition', as deposited and 2h-annealed in air). Spectra of Co-O-B as-deposited layer and of CoO, Co_3O_4 and metallic Co are reported for comparison.

agreement with XRD results, and (ii) part of Co atoms do not participate to the metallic phase, remaining oxidized likely in proximity to the particle surface, where the interaction with O atoms is favored. The Co-Co coordination distance is 2.45 Å for the as-deposited particle layer and 2.50-2.54 Å for the other cases (Table S1), to be compared with the 2.51 Å of metallic Co and ≈2.4 Å of Co_2B (see Table S1). The short coordination distance in the as-deposited particle layer suggests that a fraction of cobalt boride is present, also in agreement with XRD results. The presence of small Co clusters could also contribute to lower both the coordination number and the coordination distance of the metallic shell. About the Co-O coordination, in the particle layer the Co-O distance increases significantly (of ≈ 10%, see Table S1) from the as-deposited to the 1h-annealed particle layer, where it is compatible to the one of Co^{2+} in octahedral sites of CoO. For longer annealing times it becomes comparable to the one in the corresponding full layer and in Co_3O_4. This suggests that a strong structural modification of the oxide shell occurs in the particle layers, induced by 1-2 h air annealing. Besides the Co-O and Co-Co contributions discussed, it is worth noting the absence of any signal from medium range order in the as-deposited full layer and particle layer, showing that the as-deposited material is mostly amorphous.

To shed light on the structural and chemical modification induced by annealing in the Co-O-B PLD deposited layers, it is useful to compare the obtained information of the Co site with the XANES analysis for (i) a deposition, labeled 'Co-O layer', produced in the same conditions but without B (i.e., the PLD target used for the deposition was pure Co) and (ii) a PLD deposition, labeled 'Co layer' from a pure Co target in vacuum. The XANES spectra for the different layers are reported in Figure 7 and compared to the reference spectra of

the relevant Co oxide phases. The spectrum of the as-deposited Co-O layer is identical to the one of Co_3O_4, indicating that already in the deposition procedure Co is fully oxidized in the stable form of Co_3O_4. As expected, the XANES spectrum remains the same after air annealing (not shown), indicating that heating does not produce any relevant change on the Co site. Correspondingly, no urchin-like structure formed [24]. If the Co PLD deposition is carried out in vacuum (Co layer), the obtained spectrum of the as-deposited layer is close to the one of metallic Co, indicating that the most part of Co forms a metallic phase. Anyway, after 2 h annealing the XANES spectrum is identical to the one of Co_3O_4, proving that Co is completely oxidized. Also in this case the SEM analysis (not shown) excluded the presence of sea-urchin like structures.

4. Discussion

We have recently reported on the highly efficient catalytic activity of Co_3O_4 urchin-like nanostructures, formed by PLD of Co-O-B layers upon heating in air [4]. The structural results presented here allow to shed light on the urchin formation mechanism.

The first observation is that urchin-like particles form upon air annealing only when the PLD layer contains B. In fact, PLD deposited layers obtained from a pure Co target in either vacuum or oxygen atmosphere do not exhibit any needle growth when heated at the same temperature [24]. This indicates a relevant role of B in the formation process of hierarchical nanostructures.

The XANES results (Figure 7) indicate that if B is not present in the deposition target (Co-O deposition) the deposited layer is fully formed of stable Co_3O_4, that is not expected to evolve during the annealing performed here. At variance to that, the oxidation state of Co in a Co-O-B as-deposited layer is 2+, while a minor part of Co form metallic and boride phases. This more modest oxidation of Co in presence of B can be understood considering that B acts as an oxygen getter [25]. In fact, the formation of B-oxides is largely favored with respect to Co oxidation (the bulk enthalpy of formation of B_2O_3 is -1272 kJ/mol, to be compared with -238 kJ/mol for CoO and -910 kJ/mol for Co_3O_4). It is also known that boron and boron compounds are usually added to carbon composites to inhibit carbon oxidation at high temperature [26]. So, the effect of B addition in the deposition process is to limit the oxidation of Co and the formation of stable Co-oxide phases.

In some cases the growth of nano-needles forming urchin-like nanostructures of transition metal oxides (α-Fe_2O_3) has been explained as a selective directional growth via inter-diffusion of oxygen and metal atoms from the metallic core of the particle [9]. Anyway, for the system under investigation the needle growth cannot be likely ascribed to a diffusion mechanism alone, but the additional chemical effect of B during annealing has likely to be considered. Indeed, in the layer prepared by simple PLD of Co (Co-layer), where a Co-oxide shell certainly covers the metallic particle, the air annealing rapidly promotes the full layer oxidation (Figure 7) without the growth of nano-needles. This indicates that the oxygen diffusion through a pure Co-oxide shell towards the metallic

core is much faster than the outdiffusion of Co from the core so that, in the annealing condition used here, the diffusion process alone does not promote the growth of needles.

The results of XRD and EXAFS analyses show that the as-deposited Co-O-B layer is largely amorphous. As remarked, the average oxidation state of Co is 2+ (XANES results) and a minor fraction of metallic Co and Co boride exist (EXAFS, XANES, XRD results), mostly confined in the spheroidal particles (EXAFS and XANES results on the full layers and particle layers). In the particle layer a fraction of Co (and B) amorphous oxide is present and the short range order of oxidized Co is limited to the first Co-O shell, in agreement with the picture of a Co-oxide (or mix Co-B-oxide) phase surrounding the metallic core. This has been also previously suggested by TEM analysis [4]. The annealing promotes relevant structural modifications, in particular in the particle layer. In the first part ($\approx$ 2 h) of air annealing, a Co partial chemical reduction is induced, especially evident in the particle layer, where Co fcc coexists with a lower fraction of oxidized amorphous Co. This chemical reduction is certainly induced by the oxidation of B, likely occurring close to the particle surface, where the interaction with O is favored. As remarked above, B acts as a getter of the oxygen atoms initially bonded to Co in the layer, as well as of oxygen atoms from the annealing atmosphere. This oxidation induces a decoupling of Co and B from Co-boride (as-deposited layer) towards separate metallic Co and likely amorphous boron oxide (2 h-annealed layer). Not only the particle core, but also the oxide shell modifies during the first annealing step, as underlined by the modification of the Co-O distance in the particle layer after 1 h annealing (EXAFS results, Supplementary Material). The role of B during annealing is twofold. First, acting as a O getter, it limits oxygen diffusion into the particle core. Second, it promotes the chemical reduction of Co to the metallic phase. Then, the Co oxidation proceeds and the formation of Co_3O_4 nanoneedles is observed. About this, it is known that Co atoms in bulk Co can outdiffuse through the surface oxide layer at a temperature as low as 450 °C[27]. Oxidation of bulk Co in oxygen-rich atmosphere at moderate temperature (i.e. below 700 °C) proceeds via Co outdiffusion, that is promoted by a gradient of cation vacancy in the oxide layer between the sample surface (where the Co_3O_4 phase is formed) and the metal interface (i.e., with higher vacancy concentration at the sample surface) [27, 28, 29]. In the present nanostructured system, Co outdiffusion is likely not homogeneous on the particle surface, being favored by fast-diffusion channel in the defective Co-O-B shell, possibly formed by stress release due to the different thermal expansion coefficient of the metallic core and the oxide shell [4]. Then Co atoms that reach the particle surface oxidize. The formation of Co_3O_4 nanoneedles likely occurs via the progressive growth of the Co_3O_4 crystalline embryo feeded by the outdiffusing Co atoms. Moreover, with respect to the bulk case, the nanostructured character of the present system is expected to favor the diffusion of oxygen from the atmosphere through the layer. In this framework, as remarked above, the chemical role of B is crucial, allowing the outdiffusion of Co from the particle core to be temporary favored with respect to the diffusion of O towards the particle core. The diffusion of

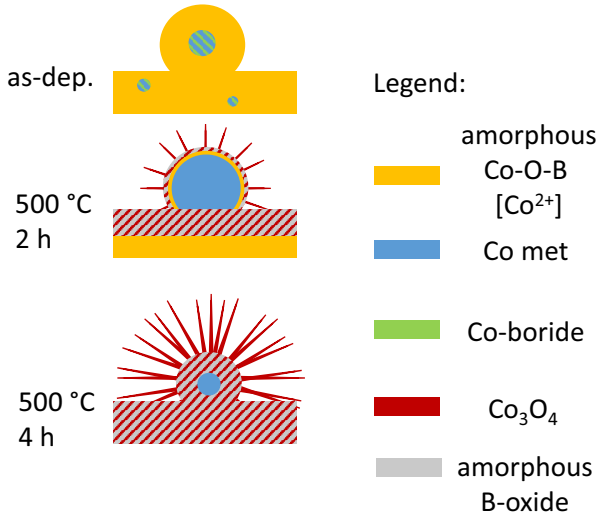

Figure 8: (Color online) Sketch of the structural evolution of Co-O-B deposited layers upon air annealing at 500 °C.

the species through the Co-O-B shell is then driven by coupled thermal and chemical effects.

The experimental results obtained suggests that the needle growth occurs from the Co outdiffusion and oxidation of a metallic reservoir. As noted above, the growth of nano-needles does not occur on the layer beneath the particles. This is likely due to the fact that the fraction of metallic Co in the layer underneath the particles is very low. Moreover, the medium range order of Co_3O_4 in the full layer is induced already after 2 h annealing (see Table S1). This indicates that the layer conformation and porosity favor a fast oxidation of Co, that prevents the formation of Co-oxide nano-needles by Co outdiffusion. In Figure 8 a sketch of structural modification induced by air annealing on Co-O-B layers is reported, summarizing the considerations above.

5. Conclusions

The growth mechanism of Co_3O_4 sea urchin-like nanostructures starting from Co-O-B layers deposited by PLD has been investigated by X-ray absorption spectroscopy, X-ray diffraction and scanning electron microscopy. After the structural characterization of the full layer annealed for different time intervals, the particles that constitute the urchin embryos have been peeled off from the substrate by embedding them in a polymer and then investigated separately. Before any annealing, the particles are formed of (amorphous) Co oxide, with a fraction of metallic Co and Co-boride. It has been demonstrated that B atoms

partially inhibit Co oxidation during the deposition process. In the first steps of air annealing, B induces a partial Co chemical reduction, especially evident in the particles, where a metallic core (Co fcc) is surrounded by an Co-O-B oxide shell. After 2 h heating Co oxidation proceeds and Co atoms outdiffuse from the Co fcc particle core likely through fast diffusion channel present in the shell and form Co_3O_4 nano-needles. The growth of nano-needles from the layer beneath the particles is prevented by a faster Co oxidation and a minimum fraction of metallic Co. This investigation shows how diffusion mechanisms and chemical effects can be effectively coupled to obtain hierarchical structures of transition metal oxides.

Acknowledgment

We acknowledge Francesco D'Acapito (BM08 beamline, CNR-IOM) for assistance during measurements, the European Synchrotron Radiation Facility (BM08 beamline) and the Italian National Research Council (CNR) for provision of beamtime.

Appendix A. Supplementary Material

The following is a Supplementary Material to this article:
EXAFS.pdf

6. References

[1] X. Li, J. Yu, M. Jaroniec, Hierarchical photocatalysts, Chem. Soc. Rev. 45 (2016) 2603–2636. doi:10.1039/C5CS00838G.
URL http://dx.doi.org/10.1039/C5CS00838G

[2] Z. Ren, Y. Guo, C.-H. Liu, P.-X. Gao, Hierarchically nanostructured materials for sustainable environmental applications, Front. Chem. 1 (2013) 1 – 22. doi:10.3389/fchem.2013.00018.
URL http://journal.frontiersin.org/article/10.3389/fchem.2013.00018/abstract

[3] J.-M. Wu, B. Huang, A. Osaka, Titania nanoflowers with high photocatalytic activity, J. Am. Ceram. Soc. 89 (2006) 2660–2663.

[4] R. Edla, N. Patel, M. Orlandi, N. Bazzanella, V. Bello, C. Maurizio, G. Mattei, P. Mazzoldi, A. Miotello, Highly photo-catalytically active hierarchical 3d porous/urchin nanostructured co_3o_4 coating synthesized by pulsed laser deposition, Applied Catalysis B: Environmental 166–167 (0) (2015) 475 – 484. doi:http://dx.doi.org/10.1016/j.apcatb.2014.11.060.
URL http://www.sciencedirect.com/science/article/pii/S0926337314007772

[5] C. M. Ling, A. R. Mohamed, S. Bhatia, Performance of photocatalytic reactors using immobilized tio$_2$ film for the degradation of phenol and methylene blue dye present in water stream, Chemosphere 57 (7) (2004) 547 – 554. doi:http://dx.doi.org/10.1016/j.chemosphere.2004.07.011.
URL http://www.sciencedirect.com/science/article/pii/S0045653504005739

[6] R. Edla, S. Gupta, N. Patel, N. Bazzanella, R. Fernandes, D. Kothari, A. Miotello, Enhanced h$_2$ production from hydrolysis of sodium borohydride using co$_3$o$_4$ nanoparticles assembled coatings prepared by pulsed laser deposition, Applied Catalysis A: General 515 (2016) 1 – 9. doi:http://dx.doi.org/10.1016/j.apcata.2016.01.031.
URL http://www.sciencedirect.com/science/article/pii/S0926860X1630031X

[7] X. Xie, W. Shen, Morphology control of cobalt oxide nanocrystals for promoting their catalytic performance, Nanoscale 1 (2009) 50–60. doi:10.1039/B9NR00155G.
URL http://dx.doi.org/10.1039/B9NR00155G

[8] T. Yu, Y. Zhu, X. Xu, Z. Shen, P. Chen, C.-T. Lim, J.-L. Thong, C.-H. Sow, Controlled growth and field-emission properties of cobalt oxide nanowalls, Advanced Materials 17 (13) (2005) 1595–1599. doi:10.1002/adma.200500322.
URL http://dx.doi.org/10.1002/adma.200500322

[9] L.-C. Hsu, H.-C. Yu, T.-H. Chang, Y.-Y. Li, Formation of three-dimensional urchin-like α-fe$_2$o$_3$ structure and its field-emission application, ACS Applied Materials & Interfaces 3 (8) (2011) 3084–3090, pMID: 21774492. arXiv:http://dx.doi.org/10.1021/am200602n, doi:10.1021/am200602n.
URL http://dx.doi.org/10.1021/am200602n

[10] L. He, Z. Li, Z. Zhang, Rapid, low-temperature synthesis of single-crystalline co$_3$o$_4$ nanorods on silicon substrates on a large scale, Nanotechnology 19 (15) (2008) 155606.
URL http://stacks.iop.org/0957-4484/19/i=15/a=155606

[11] T. Yu, Y. Zhu, X. Xu, Z. Shen, P. Chen, C.-T. Lim, J.-L. Thong, C.-H. Sow, Controlled growth and field-emission properties of cobalt oxide nanowalls, Advanced Materials 17 (13) (2005) 1595–1599. doi:10.1002/adma.200500322.
URL http://dx.doi.org/10.1002/adma.200500322

[12] Z. Dong, Y. Fu, Q. Han, Y. Xu, H. Zhang, Synthesis and physical properties of co$_3$o$_4$ nanowires, The Journal of Physical Chemistry C 111 (50) (2007) 18475–18478. arXiv:http://dx.doi.org/10.1021/jp075365l, doi:10.1021/jp075365l.
URL http://dx.doi.org/10.1021/jp075365l

[13] B. Varghese, C. Teo, Y. Zhu, M. Reddy, B. Chowdari, A. Wee, V. Tan, C. Lim, C.-H. Sow, Co_3o_4 nanostructures with different morphologies and their field-emission properties, Advanced Functional Materials 17 (12) (2007) 1932–1939. doi:10.1002/adfm.200700038.
URL http://dx.doi.org/10.1002/adfm.200700038

[14] M. Staniuk, O. Hirsch, N. Kränzlin, R. Böhlen, W. van Beek, P. M. Abdala, D. Koziej, Puzzling mechanism behind a simple synthesis of cobalt and cobalt oxide nanoparticles: In situ synchrotron x-ray absorption and diffraction studies, Chemistry of Materials 26 (6) (2014) 2086–2094. arXiv:http://dx.doi.org/10.1021/cm500090r, doi:10.1021/cm500090r.
URL http://dx.doi.org/10.1021/cm500090r

[15] C. Maurizio, N. El Habra, G. Rossetto, M. Merlini, E. Cattaruzza, L. Pandolfo, M. Casarin, Xas and gixrd study of co sites in $coal_2o_4$ layers grown by mocvd, Chemistry of Materials 22 (5) (2010) 1933–1942. arXiv:http://dx.doi.org/10.1021/cm9018106, doi:10.1021/cm9018106.
URL http://dx.doi.org/10.1021/cm9018106

[16] C. Maurizio, R. Checchetto, A. Trapananti, A. Rizzo, F. D'Acapito, A. Miotello, In situ x-ray absorption spectroscopy-x-ray diffraction investigation of nb-h nanoclusters in mgh_2 during hydrogen desorption, The Journal of Physical Chemistry C 119 (14) (2015) 7765–7770. arXiv:http://dx.doi.org/10.1021/acs.jpcc.5b00252, doi:10.1021/acs.jpcc.5b00252.
URL http://dx.doi.org/10.1021/acs.jpcc.5b00252

[17] D.-H. Ha, L. M. Moreau, S. Honrao, R. G. Hennig, R. D. Robinson, The oxidation of cobalt nanoparticles into kirkendall-hollowed coo and co_3o_4: The diffusion mechanisms and atomic structural transformations, The Journal of Physical Chemistry C 117 (27) (2013) 14303–14312. arXiv:http://dx.doi.org/10.1021/jp402939e, doi:10.1021/jp402939e.
URL http://dx.doi.org/10.1021/jp402939e

[18] N. Patel, A. Miotello, V. Bello, Pulsed laser deposition of co-nanoparticles embedded on b-thin film: A very efficient catalyst produced in a single-step process, Applied Catalysis B: Environmental 103 (1) (2011) 31 – 38. doi:http://dx.doi.org/10.1016/j.apcatb.2011.01.005.
URL http://www.sciencedirect.com/science/article/pii/S0926337311000142

[19] C. C. M. Bonelli, A. Miotello, Pulsed laser deposition apparatus for applied research, Meas. Sci. Techn. 10 (1999) N27.

[20] L. Lutterotti, D. Chateigner, S. Ferrari, J. Ricote, Texture, residual stress and structural analysis of thin films using a combined x-ray analysis, Thin Solid Films 450 (1) (2004) 34 – 41. doi:http://dx.doi.org/10.1016/j.tsf.2003.10.150.
URL http://www.sciencedirect.com/science/article/pii/S0040609003014329

[21] B. Ravel, M. Newville, Athena, artemis, hephaestus: Data analysis for x-ray absorption spectroscopy using ifeffit, Journal of Synchrotron Radiat. 12 (4) (2005) 537–541. doi:10.1107/S0909049505012719.
URL http://dx.doi.org/10.1107/S0909049505012719

[22] B. Liu, H. Zeng, Symmetric and asymmetric ostwald ripening in the fabrication of homogeneous core-shell semiconductors, Small 1 (5) (2005) 566–571. doi:10.1002/smll.200500020.
URL http://dx.doi.org/10.1002/smll.200500020

[23] E. Havinga, H. Damsma, P. Hokkeling, Compounds and pseudo-binary alloys with the cual$_2$(c16)-type structure i. preparation and x-ray results, Journal of the Less Common Metals 27 (2) (1972) 169 – 186. doi:http://dx.doi.org/10.1016/0022-5088(72)90028-8.
URL http://www.sciencedirect.com/science/article/pii/0022508872900288

[24] T. Warang, N. Patel, A. Santini, N. Bazzanella, A. Kale, A. Miotello, Pulsed laser deposition of co$_3$o$_4$ nanoparticles assembled coating: Role of substrate temperature to tailor disordered to crystalline phase and related photocatalytic activity in degradation of methylene blue, Applied Catalysis A: General 423–424 (2012) 21 – 27. doi:http://dx.doi.org/10.1016/j.apcata.2012.02.037.
URL http://www.sciencedirect.com/science/article/pii/S0926860X1200110X

[25] K. Elers, V. Saanila, S. Kaipio, P. Soininen, Production of elemental thin films using a boron-containing reducing agent, uS Patent 6,475,276 (Nov. 5 2002).

[26] Y. Wang, J. Fan, M. Trenary, Surface chemistry of boron oxidation. 1. reactions of oxygen and water with boron films grown on tantalum(110), Chemistry of Materials 5 (2) (1993) 192–198. arXiv:http://dx.doi.org/10.1021/cm00026a007, doi:10.1021/cm00026a007.
URL http://dx.doi.org/10.1021/cm00026a007

[27] K. A. E.A. Gulbransen, The kinetics of the oxiation of cobalt, J. Electrochem. Soc. 88 (1951) 241.

[28] R. E. Carter, F. D. Richardson, C. Wagner, Oxidation of cobalt metal, JOM 7 (2) (1955) 336–343. doi:10.1007/BF03377503.
URL http://dx.doi.org/10.1007/BF03377503

[29] Z. G. Kaczmarska, A., S. Mrowec, On the defect structure and transport properties of co$_3$o$_4$ spinel oxide, High Temp. Mater. Proc. 31 (2012) 371.